COMBINED CLOSE RANGE PHOTOGRAMMETRY AND REMOTE SENSING FOR PHOTOVOLTAIC PARKS EFFICIENCY ANALYSIS

A. S. Yordanov[1], D. G. Filipov[1], S. L. Katsarska-Filipova[1], Ts. P. Atanasova[1]

[1]University of Architecture, Civil Engineering and Geodesy (UACEG), Faculty of Geodesy, Dept. of Photogrammetry and Cartography, Sofia, Bulgaria – (gfac.4959, filipov_fgs, filipova_fgs, tsatanasova_fgs)@uacg.bg

KEY WORDS: close-range photogrammetry, remote sensing methods, multichannel image, supervised classification, orthoimages.

ABSTRACT:

The paper presents an innovative approach of combining the methods of close-range photogrammetry and remote sensing in the analysis of the efficiency of photovoltaic parks. A UAV was used to capture the site and close-range photogrammetry technology was used to create orthoimages in the thermal and visible zone. Orthoimages obtained from close-range photogrammetry imagery were combined, and the resulting multichannel image was analysed with remote sensing methods. Spatially overlapping RGB and thermal orthoimages are collocated and a multispectral image was created. Cluster analysis of the multispectral image was performed. Using remote sensing methods, a four-channel multichannel image was created and classified through supervised classification approach with predefined masks. The training data for the classifier represents the types of defects found on the photovoltaic panels. The obtained results were analysed and an assessment of the classification was made.

1. INTRODUCTION

Aerial photogrammetry uses different methods to extract information from images. Methods of traditional photogrammetry, close-range as well as remote sensing are applied. These methods allow extraction of multi-layered information using multichannel images. Each channel of these images contains different information because of the way they are formed. Each channel represents an image of the scene, but in a different spectral range. After that, by combining the individual channels, different information about the captured area can be extracted.

This paper will introduce an innovative method to create a multichannel image by using two orthoimages of the same area. The new image combines the most important features from the two separate images and provides new possibilities for terrain analysis.

The objective of the analysis is to automatically identify problem areas in the photovoltaic park. For this purpose, a supervised classification is used on the multichannel image. The final results are compared with those determined on site and the classification is evaluated.

2. EQUIPMENT AND SITE CHARACTERISTICS

The difficulty of finding and tracking down problems and potential issues that arise in these installations is monumental. Therefore Infrared thermography is a valuable technology that can be used on a wider scale to pinpoint problems in these large arrays (Denio H., 2012). Photogrammetric processing of close-range thermal infrared (TIR) images deals with several challenging difficulties. The resolution of TIR images is much lower compared to the resolution of images captured by common digital RGB cameras. The field of view (FOV) of thermal infrared cameras is generally much narrower (Dlesk A. at all, 2021).

The captured photovoltaic park is located near the city of Pazardzhik, Bulgaria (Figure 1). The solar panels are located on an area of 6 hectares. Due to the large number of panels, it is more appropriate to use unmanned aerial vehicles equipped with a thermographic camera.

For the purposes of the analysis, the photovoltaic park was captured by a YUNEEC H520E unmanned aerial vehicle (Figure 2). The aircraft is classified as UAVs with rotor blades. It flies fully autonomously, with a flight plan set from the ST16S "remote control" ground station.
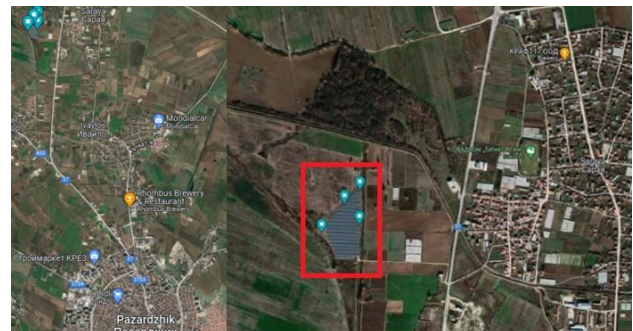

Figure 1. Area of interest - 42.246178, 24.306225 Pazardzhik Municipality.

Figure 2. Unmanned aerial vehicle.

An E20Tvx camera was used which is a combination of a thermal and a RGB camera attached to the Gimbal (Figure 3).

Figure 3. Thermal and a RGB camera

Weight	365g
Infrared Part	
Sensitivity	<50mk@F1.0/20°C
Infrared Wavelength Range	8-14μm
Frequency Full Frame Rate	25Hz
Resolution	640×512
Lens	13mm f/1.0, HFOV32°
Temperature Measurement Range	-20° to 150°
Optical Part	
Sensor	1/2.8" 2M
Equivalent Focal Length	23mm
Resolution	1920x1080

Table 1. Camera parameters

In the flight plan settings, the following are set: speed, altitude and flight range. A flight height of 75m with a longitudinal overlap of 60% was used for the analysis. The value of the GSD is 7cm, for the thermal channel, which is quite enough to perform the analysis, because the cells of the solar modules are 15x15cm in size. When using the thermographic camera, the stop-and-shoot option was used. This option causes the aircraft to pause for a few seconds to properly expose the image.

To ensure the correct geometry of the site, which serves to create the orthoimages, 5 ground control points marked with photogrammetric marks are placed on the terrain. Control points are marked on the field with combined marks with a standard 20x20cm L-shaped element for RGB imaging, and a square element with a highly reflective coating for easier detection of the points in thermographic images. To determine the coordinates of the points, the measurements were made with a Hi-Target V200 GNSS receiver. VRS (Virtual Reference Station) mode was used. For each point, a fixed solution was obtained in RTK-mode using a GeoVara permanent reference grid. The accuracy of the receiver in plan is 5mm+0.5ppm, and in height – 10mm=0.5ppm. The coordinates of the internal corner of the "L" shaped marks for the RGB capture are determined, which coincide with the corresponding peak of the thermal mark.

3. THERMOGRAPHIC IMAGING. ORTHOIMAGES GENERATION (RGB AND THERMAL) - ACCURACIES AND RESULTS

By definition thermographic images are based on capturing the emitted electromagnetic radiation from an object with a temperature higher than absolute zero. The emitted radiation spreads through the atmosphere and can be captured using an instrument with a suitable sensor, such as a thermal infrared camera. The sensor captures the radiation in a certain range and records its intensity. Given the parameters of the object and its surroundings, the device can calculate the temperature of the surface.

The physical principles of thermography were discovered and described as early as 1900 by the scientists Max Planck, Joseph Stephan, Ludwig Boltzmann, Wilhelm Wien and Gustav Kirchov. To describe the mentioned principles, the so-called "absolute black body" is defined. It is an abstract physical body that absorbs and emits 100% of the energy (including radiation) with which it is irradiated.

$\alpha = \varepsilon = 1$ (α – absorption coefficient, ε – emissivity coefficient)
The absolute black body emits the maximum amount of energy in the entire electromagnetic spectrum.

The basic connection between spectral emissivity, blackbody temperature, and wavelength are described in Planck's law of radiation. According to this law, the specific spectral radiation of the blackbody is determined by the following formula:

$$M_{0\lambda} = \frac{2\pi hc^2}{\lambda^5} \frac{1}{e^{\frac{hc}{\lambda kT}}-1} = \frac{C_1}{\lambda^5} \frac{1}{e^{\frac{c_2}{\lambda T}}-1} \qquad (1)$$

where:
c = the speed of light;
C_1 = 3.74*10-10 W m2;
C_2 = 1.44*10-2 K m;
h = Planck's constant;
k = Boltzmann constant.

All emitted radiation from the black body in the entire spectrum increases proportionally to the 4th power of the body's absolute temperature (Edelman G.J. at all, 2013). Also, according to the graphic representation of Planck's law, the wavelength that causes the black body to emit maximum changes as the temperature changes. This dependence is explained by Wien's displacement law:

$$\lambda_{max}T = 2898\mu mK \qquad (2)$$

Unlike an absolute black body, real objects do not radiate all their energy. When it comes to them the specific spectral radiation is determined by the formula:

$$M_\lambda = \varepsilon_\lambda M_{0\lambda} \qquad (3)$$

where:
ε_λ is the spectral emissivity of the object.

The emissivity value takes values between 0 and 1, with a black body having an emissivity equal to 1. The emissivity depends on various factors such as the wavelength of the irradiating energy, temperature and material from which the object is made, as well as the angle of monitoring. However, there are objects whose emissivity can be considered constant in certain wavelength ranges.

In the case of indirect temperature measurements, an instrument and an infrared sensor are placed in front of the object under study. The object has a certain temperature T_{obj} and is made of a material with emissivity ε_{obj}.. The object emits its own energy in the form of a radiant flux εI_{obj}. This energy passes through the atmosphere with a coefficient of conductivity τ_{ATM} so that the beam flux reaches the instrument. In addition to radiation from the object, all surrounding objects also radiate energy to the object under study, which is subsequently reflected from the object and passes through the atmosphere. Thus, the beam flux entering the instrument is $(1-\varepsilon) \tau I'_{REF}$. The

atmosphere also has its own radiative flux $(1-\tau)\, I^{'}_{ATM}$. The sum of these three ray fluxes is called the equation of thermography, and using the knowledge of the above laws it is possible to determine the temperature of the surface of the studied object. It is important to note that the determination of parameters such as the emissivity of the object, the reflected temperature, and the conductivity and temperature of the atmosphere are of utmost importance in determining the surface temperature of the body. Finally, the equations for body temperature and total temperature can be written as follows:

$$I^{'}_{TOTAL} = \varepsilon\tau I^{'}_{OBJ} + (1-\varepsilon)\tau I^{'}_{REF} + (1-\tau)I^{'}_{ATM} \tag{4}$$

$$I^{'}_{OBJ} = 1\varepsilon\tau I^{'}_{TOTAL} - 1 - \varepsilon\varepsilon I^{'}_{REF} - 1 - \tau\varepsilon\tau I^{'}_{ATM} \tag{5}$$

In the study of photovoltaic panels, the dependence on the state of each photovoltaic cell is applied for the change in its temperature.

In the traditional study of the potential of photovoltaic panels, thermal and optical images are used separately. The proposed technology makes it possible to perform an in-depth analysis after combining the generated orthorectified images for the thermal and visible spectral range.

Captured images were obtained as center projection. In order to obtain the correct geometry and characteristics of the object, it is necessary to transform them into an orthogonal projection. For this purpose, it is necessary to know the orientation parameters of each image, as well as to have a 3D model of the captured surface. The transformation of the source image is performed by transforming each pixel, taking into account its height position. In this way, we get orthoimages from which an orthophotomosaic is created.

Two orthoimages are generated from the captured RGB and thermal images. Agisoft Metashape Professional software is used for processing. To create the orthoimages, the methods of traditional photogrammetry related to internal and external (relative and absolute) orientation were applied.

In the georeferencing (absolute orientation) of the orthoimages, the following accuracies were achieved:

Markers	Accuracy (m)	Error (m)	Error (pix)
pt1	0.005	0.004	0.227
pt2	0.005	0.003	0.335
pt3	0.005	0.008	0.186
pt4	0.005	0.006	0.425
pt5	0.005	0.005	0.398
Total Error			
Control points		0.004	0.393

Table 2. Accuracy of the thermal orthoimages

For RGB images – Table. 3

Label	X error (m)	Y error (m)	Z error (m)	Total (m)	Image (pix)
pt1	0.001	-0.006	-0.002	0.006	0.2 (19)
pt2	-0.005	0.001	-0.002	0.005	0.1 (12)
pt3	-0.005	0.005	0.006	0.005	0.2 (21)
pt4	0.009	-0.001	-0.003	0.002	0.2 (15)
pt5	0.001	0.003	0.002	0.003	0.1 (28)
Total	**0.005**	**0.004**	**0.003**	**0.004**	**0.2**

Table 3. Accuracy of the RGB orthoimages

The accuracies of the two orthoimages are presented as follows in the table. 2 for the thermal orthoimage and table 3 for the RGB orthoimage. Techniques of image correlation are used in point identification.

4. CREATING MULTICHANNEL IMAGE, MASKING, PRELIMINARY ASSESSMENT AND DEFECT CLUSTERING, CLASSIFIERS, CLASSIFICATION.

A multispectral image is a digital image, where each pixel includes multiple DNs (digital number), one for each spectral band. When viewing this multi-band image, it is possible to view a single band at a time, treating it as if it were a discrete image, with brightness values proportional to DN. Alternatively, and more commonly, three bands from the image can be selected and displayed simultaneously in shades of red, green, and blue, to create a color composite image, whether on a computer monitor or in a hard copy print (Jonathan W. Chipman, 2015).

In our case a multispectral image is created through combining both spatially overlapping orthoimages. Collocating products implies that the pixel values of slave products are resampled into the geographical raster of the master product. In order to avoid naming conflicts, both master and slave components such as bands, flag coding and bitmask definitions are renamed according to a user defined pattern.

A new product is created which contains a copy of all components of the master product, and all components of the slave products are transferred in a different manner. The band data of the slave products are resampled into the geographical raster of the master product. For resampling method, flag bands and bands where a valid-pixel expression is defined, the Nearest Neighbor method is used. In order to establish a mapping between the samples in the master and the slave rasters, the geographical position of a master sample is used to find the corresponding sample in the slave raster. Accurate geopositioning information for both master and slave products is necessary for collocation algorithm. Slave product metadata are not transferred.

Techniques used in the processing of satellite images were used to collocate the images and analyse the results. With the two orthoimages and the capabilities of the SNAP software, a multichannel image is created. For this purpose, both images are in the same coordinate system. By fulfilling these requirements and applying a "collocation" algorithm, a multichannel image with 4 channels is created. A new product is created which contains a copy of all components of the master product - in our case, the color orthoimage. The band data of the thermal orthoimage are resampled into the geographical raster of the master product. It's applied Nearest Neighbour resampling method. Accurate geolocation information for both master and slave products is used to implement the Colocation Algorithm.

The need to create a multi-channel image follows from the structure of the solar panels. The panels consist of solar cells and frames. The frames are made of aluminium, whose good thermal conductivity causes it to heat up to a temperature close to that of a working solar cell. This causes the frames and cells to "merge" at the thermal channel of the multichannel image. But in addition to good thermal conductivity, aluminium has excellent reflectivity in the visible range (significantly higher than that of solar cells), which makes it easily distinguishable on a colour image. If only a thermal image is used, inaccuracies occur in distinguishing the different problem areas. In the thermal image, the problematic photovoltaic elements are clearly distinguished, in contrast to the RGB image, where they are difficult to distinguish.

The orthoimages contain both the solar park panels and the ground base, security staff cabins and other side features outside the park boundaries. Masks are created to separate the solar panels from the rest of the elements in the images. The masks completely cover the area of the panels. As a result of masking, only the areas occupied by solar panels remain from the image.

A preliminary assessment of the different possible states of the photovoltaic panels has been made. Based on the collected-on site information about the defects the following types were distinguished:
- Working panels
- Non-current producing panels (string connection fault)
- Broken panels (physical defect)
- Shaded panels and frames
Cluster analysis with the following parameters was used for preliminary image evaluation:
– Number of object classes – 4 – the number of predefined panel types
– Number of iterations – 30
– Mask – the panel mask is used

In order to standardize the results and facilitate comparisons the following colours have been assigned to the classes:
- Broken panels – red
- Non-current producing panels - grey
- Working panels – green
- Shaded panels and frames - blue
As a result, two subsets are presented - from an area with broken panels and an area with panels not producing current (the areas were determined during the field survey):
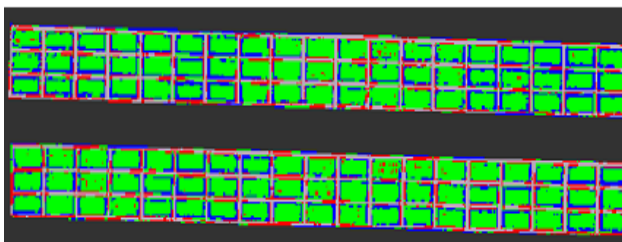

Figure 4. Result from Cluster analysis – Green (Working panels), Red (Broken panels), Blue (Frames), Gray (Non-current producing panels)

Based on the cluster analysis several problems arise (Figure 4):
- It is not possible to unambiguously define the boundaries of the panels to one class. Pixels representing the frames fall into several classes
- It is not possible to unambiguously determine the panels that do not produce current from the working panels
- It is not possible to unambiguously distinguish the broken panels from the working panels
Thus, it is necessary to create vector containers for the predefined panel types. When creating the classifier, the pixels where any of the defects are present are precisely marked. For each class, several vector containers where the corresponding defect is present are created to ensure their correct classification.

Then we estimated the quality of all vector containers with the statistics tool in SNAP. This tool extracts pixel values in different bands and uses the vector containers as mask layers. This allows analysing the behaviour of the etalons and choosing the right bands for further classification. Results of the analysis is presented below (fig. 5, 6, 7 and 8).
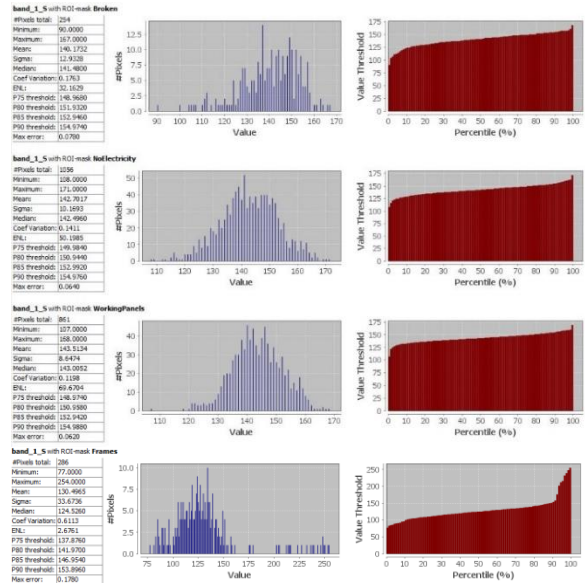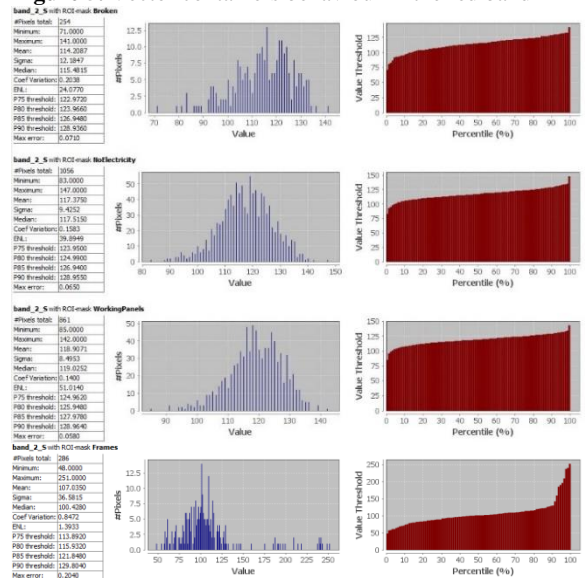

Figure 5. Vector containers behaviour in the red band

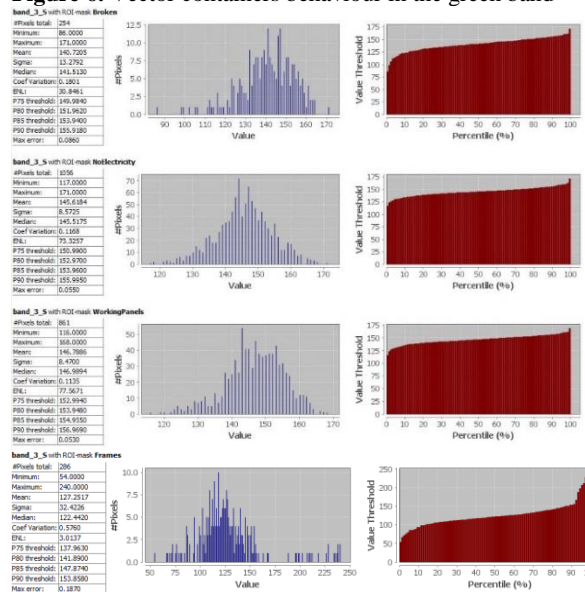**Figure 6.** Vector containers behaviour in the green band

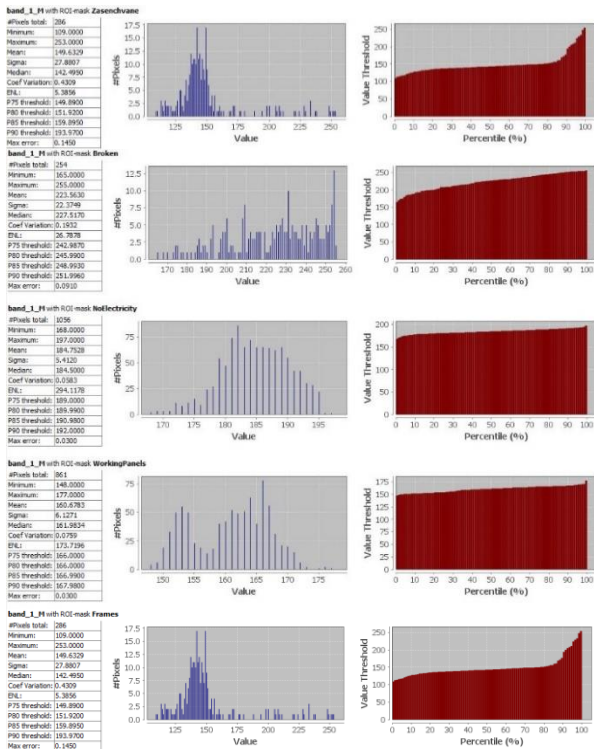**Figure 7.** Vector containers behaviour in the blue band

Figure 8. Vector containers behaviour in the thermal band

As conclusion from the analysis, we can say that all of the defects are easily distinguishable in the thermal band and the frames are distinguishable in the red, blue and green bands. That's why we used all of the bands in the further classification.

A supervise classification was done using Random Forest algorithm. The following parameters were used for the classification:

– Number of vector containers used for the classifier – 5000.
– Number of trees – 10
– Number of classes - 4
– Feature bands – 4 channels

During the classification, a new classifier was created. The classification was evaluated with 100 randomly selected points. Part of the selected random points for the evaluation is presented in the Appendix 1.

As a result, two subsets are again presented in areas with broken panels and areas with panels not producing current.
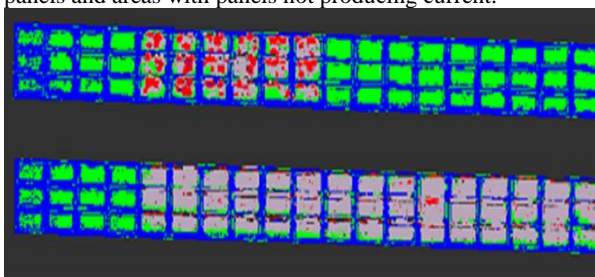

Figure 5. Result from supervised classification using Random Forest algorithm - Green (Working panels), Red (Broken panels), Blue (Frames), Gray (Non-current producing panels)

The following changes are noticeable from the new classification (Figure 5):
- Panel frames and shading are classified in separate classes
- The panels not producing current are classified into a separate class different from that of the working panels
- Broken panels are classified into a separate class and are easily distinguishable

- The classified image can be used for further research, as supplementary material.

5. EVALUATION OF THE CLASSIFICATION, RESULTS, CONCLUSIONS

Both classification approaches were evaluated to verify the accuracy of the final result. For this purpose, points were randomly selected and tools for the statistical analysis of compliance were used. The points have a specific name and coordinates that take on the properties of the class they fall into when transferred onto the classified image. They are evenly distributed across the site and fall into each of the 4 panel types (broken, non-working, shaded/framed and working) using the multichannel image and field survey data.

Two types of data regarding the points for the evaluation is derived - visually determined class of the pixel and actual class in the classified image. An analysis was made of how many of the points fell into the correct class and what number fell into the wrong class. This analysis leads to several important conclusions. How reliable is the image collocation algorithm, how reliable is the classification, which classes are difficult to distinguish in automated processing and can the final product of the classification serve as a basis for further research related to the efficiency of the particular photovoltaic park.

The evaluation of the classification made with the Random Forest algorithm leads to the establishment of 92.50% correspondence with the real class. From this result it can be concluded that:

- The technology for collocation of orthoimages of different spectral ranges is an effective method for in-depth analyses in various fields, which leads to very good results
- Supervised classification of multichannel images obtained by combining two or more orthoimages from different sensors and long wavelengths is not only possible, but the achieved results are of very high accuracy
- The biggest difficulties and errors occur during the classification of the class representing the broken panels. In this class, 20% of tags are recognized as "non-current producing", 10% as "Working", and 70% are correctly recognized. The reason lies in the specificity of the class. With physical breaks present, the area around the break does not produce current and falls into the "non-current producing" class, with very little break around it, it continues to produce current, leading to it being recognized as "Working".

	Broken	Non-current producing	Working	Shaded/Frame	Classified correctly	Total
Broken	70	0	0	0		100
Non-current producing	20	100	0	0		100
Working	10	0	100	0		100
Shaded/Frame	0	0	0	100		100
Classified correctly					370	Accuracy
Total.	100	100	100	100	400	92.50 %

Table 4. Accuracy of the classification based on 100 random points.

REFERENCES

Dlesk A., Vach K., Pavelka K., 2022: Photogrammetric Co-Processing of Thermal Infrared Images and RGB Images, *Sensors (Basel)*, Published online 2022 Feb 20. DOI: 10.3390/s22041655.

Dlesk A., Vach K., Pavelka K., 2021: Transformations in the Photogrammetric Co-Processing of Thermal Infrared Images and RGB Images, *Sensors (Basel)*, Published online 2021 Jul 26. DOI: 10.3390/s21155061.

Denio H., 2012: Aerial solar Thermography and condition monitoring of photovoltaic systems, *IEEE Xplore: 04 October 2012*, 38th IEEE Photovoltaic Specialists Conference, DOI: 10.1109/PVSC.2012.6317686.

Sledz, A.; Unger, J.; Heipke, C., 2018: Thermal IR imaging: Image quality and orthophoto generation. In: *International Archives of the Photogrammetry, Remote Sensing and Spatial Information Sciences* - ISPRS Archives 42 (2018), Nr. 1, S. 413-420. DOI: https://doi.org/10.5194/isprs-archives-XLII-1-413-2018.

Gade, R., Moeslund, T.B., 2014: Thermal cameras and applications: a survey. *Machine Vision and Applications* 25, 245–262 (2014). DOI:https://doi.org/10.1007/s00138-013-0570-5.

Norman J. W. Thrower &John R. Jensen, 2013: The Orthophoto and Orthophotomap: Characteristics, Development and Application, *The American Cartographer*, Pages 39-56 | Published online: 14 Mar 2013, DOI: https://doi.org/10.1559/152304076784080249.

Liang-Chien Chen, Tee-Ann Teo, Chien-Liang Liu, Rigorous Georeferencing for Formosat-2 Satellite Images by Least Squares Collocation, *Center for Space and Remote Sensing Research,* National Central University, Taiwan, 0-7803-9051-2/05/(C) 2005 IEEE

Edelman G.J., Hoveling R.J.M., Roos M., Leeuwen T.G., Aalders M.C.G. Infrared Imaging of the Crime Scene: *Possibilities and Pitfalls*. J. Forensic Sci. 2013;58:1156–1162. doi: 10.1111/1556-4029.12225.

Thomas M. Lillesand, Ralph W. Kiefer, Jonathan W. Chipman. *Remote sensing and image interpretation, Seventh edition;* ISBN 978-1-118-34328-9

APPENDIX

Appendix.1. Part of the selected random points

Name	LabeledClasses	X	Y	Lon	Lat	Name	LabeledClasses
Pin 23	Working	1247,5	4233,5	24,30534	42,24613	Pin 23	Working
Pin 1	Non-current producing	1287,5	3348,5	24,30536	42,24660	Pin 1	Non-current producing
Pin 25	Working	1353,5	4458,5	24,30542	42,24601	Pin 25	Working
Pin 24	Working	1372,5	4127,5	24,30543	42,24619	Pin 24	Working
Pin 2	Non-current producing	1663,5	3344,5	24,30563	42,24660	Pin 2	Non-current producing
Pin 20	Working	1691,5	6239,5	24,30568	42,24507	Pin 20	Non-current producing
Pin 21	Working	1722,5	6127,5	24,30570	42,24513	Pin 21	Non-current producing
Pin 22	Working	1730,5	6019,5	24,30570	42,24519	Pin 22	Working
Pin 10	Working	1769,5	2901,5	24,30570	42,24684	Pin 10	Working
Pin 9	Broken	1776,5	2824,5	24,30570	42,24688	Pin 9	Broken
Pin 11	Non-current producing	1848,5	4800,5	24,30577	42,24584	Pin 11	Non-current producing
Pin 8	Broken	1856,5	2793,5	24,30576	42,24690	Pin 8	Non-current producing
Pin 7	Broken	1911,5	2712,5	24,30580	42,24694	Pin 7	Working
Pin 27	Working	1923,5	3809,5	24,30582	42,24636	Pin 27	Working
Pin 12	Non-current producing	1963,5	4802,5	24,30586	42,24584	Pin 12	Non-current producing
Pin 18	Working	1983,5	5470,5	24,30588	42,24548	Pin 18	Working
Pin 26	Working	1997,5	4030,5	24,30587	42,24624	Pin 26	Working
Pin 40	Broken	2018,5	2483,5	24,30587	42,24706	Pin 40	Broken
Pin 41	Broken	2049,5	2468,5	24,30589	42,24707	Pin 41	Broken
Pin 16	Non-current producing	2094,5	5473,5	24,30596	42,24548	Pin 16	Non-current producing
Pin 45	Working	2108,5	5804,5	24,30597	42,24531	Pin 45	Working
Pin 19	Non-current producing	2113,5	6247,5	24,30598	42,24507	Pin 19	Non-current producing

Pin 17	Working	2115,5	5583,5	24,30597	42,24542	Pin 17	Working
Pin 15	Non-current producing	2158,5	4810,5	24,30599	42,24583	Pin 15	Working
Pin 46	Shaded/Frame	2239,5	5691,5	24,30606	42,24537	Pin 46	Shaded/Frame
Pin 13	Non-current producing	2241,5	4796,5	24,30605	42,24584	Pin 13	Non-current producing
Pin 44	Non-current producing	2280,5	5697,5	24,30609	42,24536	Pin 44	Non-current producing
Pin 14	Non-current producing	2330,5	4827,5	24,30612	42,24582	Pin 14	Non-current producing
Pin 47	Shaded/Frame	2412,5	5039,5	24,30618	42,24571	Pin 47	Shaded/Frame
Pin 50	Shaded/Frame	2527,5	2169,5	24,30623	42,24723	Pin 50	Shaded/Frame
Pin 49	Shaded/Frame	2657,5	1825,5	24,30632	42,24741	Pin 49	Shaded/Frame
Pin 31	Working	2791,5	2390,5	24,30642	42,24712	Pin 31	Working
Pin 29	Working	2866,5	3056,5	24,30648	42,24677	Pin 29	Working
Pin 30	Working	2896,5	3611,5	24,30651	42,24647	Pin 30	Working
Pin 38	Working	2989,5	6284,5	24,30660	42,24506	Pin 38	Working
Pin 39	Working	3012,5	5162,5	24,30661	42,24565	Pin 39	Working
Pin 32	Working	3080,5	2175,5	24,30662	42,24723	Pin 32	Working
Pin 37	Working	3100,5	5719,5	24,30667	42,24536	Pin 37	Working
Pin 36	Working	3229,5	5958,5	24,30677	42,24523	Pin 36	Working
Pin 43	Working	3306,5	3842,5	24,30680	42,24635	Pin 43	Working
Pin 42	Working	3403,5	3606,5	24,30687	42,24648	Pin 42	Working
Pin 33	Non-current producing	3412,5	1739,5	24,30686	42,24747	Pin 33	Non-current producing
Pin 48	Shaded/Frame	3490,5	3285,5	24,30693	42,24665	Pin 48	Shaded/Frame
Pin 6	Working	3497,5	1190,5	24,30691	42,24776	Pin 6	Working
Pin 35	Working	3532,5	2186,5	24,30695	42,24723	Pin 35	Working
Pin 28	Non-current producing	3672,5	4499,5	24,30707	42,24601	Pin 28	Non-current producing
Pin 5	Working	3703,5	990,5	24,30706	42,24786	Pin 5	Working
Pin 34	Working	3736,5	1527,5	24,30708	42,24758	Pin 34	Working
Pin 3	Non-current producing	3744,5	749,5	24,30708	42,24799	Pin 3	Non-current producing
Pin 4	Working	3764,5	863,5	24,30710	42,24793	Pin 4	Working